University of Hertfordshire UH

Document Version: Accepted Version

Link to the final published version available at the publisher:

The applicability of physical optics in the millimetre and sub-millimetre spectral region. Part II: Application to a three-component model of ice cloud and its evaluation against the bulk single-scattering properties of various other aggregate models

Anthony J. Baran[a],*, Hiroshi Ishimoto[b], Odran Sourdeval[c] , Evelyn Hesse[d], Chawn Harlow[a]

[a]*Met Office, Exeter, UK*
[b]*Meteorological Research Institute, Nagamine 1-1, Tsukuba 305-0052, Japan*
[c]*Institute of Meteorology, Universität Leipzig, Leipzig, Germany*
[d]*University of Hertfordshire, Centre for Atmospheric and Instrumentation Research, Hatfield, Hertfordshire AL10 9A, UK*

31st October 2017

*Correspondence to: Met Office, Cordouan 2, FitzRoy Road, Exeter, Devon EX1 3PB, UK.
Tel: +44 1392 886162
E-mail address: anthony.baran@metoffice.gov.uk

ABSTRACT

The bulk single-scattering properties of various randomly oriented aggregate ice crystal models are compared and contrasted at a number of frequencies between 89 and 874 GHz. The model ice particles consist of the ten-branched plate aggregate, five-branched plate aggregate, eight-branched hexagonal aggregate, Voronoi ice aggregate, six-branched hollow bullet rosette, hexagonal column of aspect ratio unity, and the ten-branched hexagonal aggregate. The bulk single-scattering properties of the latter two ice particle models have been calculated using the light scattering methods described in Part I, which represent the two most extreme members of an ensemble model of cirrus ice crystals. In Part I, it was shown that the method of physical optics could be combined with the T-matrix at a size parameter of about 18 to compute the bulk integral ice optical properties and the phase function in the microwave to sufficient accuracy to be of practical value. Here, the bulk single-scattering properties predicted by the two ensemble model members and the Voronoi model are shown to generally bound those of all other models at frequencies between 89 and 874 GHz, thus representing a three-component model of ice cloud that can be generally applied to the microwave, rather than using many differing ice particle models. Moreover, the Voronoi model and hollow bullet rosette scatter similarly to each other in the microwave. Furthermore, from the various comparisons, the importance of assumed shapes of the particle size distribution as well as cm-sized ice aggregates is demonstrated.

KEYWORDS: Electromagnetic scattering; aggregates; ice; microwave; particle size distribution, physical optics, remote sensing, single-scattering; sub-millimetre; Voronoi tessellation.

1. Introduction

There is a need to generate the bulk single-scattering properties of ice crystals in the millimetre and sub-millimetre parts of the spectrum, owing to the launch in the early 2020s of the space-based Ice Cloud Imager (ICI) instrument [1]. Moreover, these properties are also required to facilitate interpretation of multi-frequency radiometer data from the ICI airborne demonstrator instrument called the International Sub-millimetre Airborne Radiometer (ISMAR) [2]. The purpose of these instruments is to, partly, make use of their sensitivity to the presence of cirrus and ice cloud, so that properties such as column-integrated ice water content (IWC), called the ice water path (IWP), and bulk ice particle size can be retrieved from polarised multi-frequency observations. It has been known since circa 1990s that the microwave and sub-millimetre spectral regions are particularly sensitive to the IWP and bulk ice crystal size [3–6]. This sensitivity is due to ice at these frequencies being relatively weakly absorbing, thereby causing incident microwave radiation from beneath the cirrus to be scattered out of the line of sight of the instrument. This scattering process leads to depressions in the above-cirrus or ice cloud measured brightness temperature relative to the clear-sky brightness temperature, and it is these brightness temperature depressions that are known to be directly proportional to the IWP [3].

The IWP is related to a numerical weather prediction (NWP) and climate model prognostic variable, IWC. Currently, the performance of such general circulation models (GCMs) in predicting the global distribution of IWC and/or the IWP is known to be poor; see, for example, the studies described in Refs. [7–9]. Indeed, in the most recent report of the International Panel on Climate Change (IPCC) the following is stated on page 589: "representation of cirrus in GCMs appears to be poor" [10]. With such a poor representation of cirrus and/or ice mass in GCMs, which, in turn, feeds through to the representation of the hydrological cycle, there is a clear need for more direct global observations of the IWP and ice cloud microphysics through the utilisation of sub-millimetre-wave observations.

To make use of future sub-millimetre global observations of cirrus requires the further development of bulk single-scattering properties of observed atmospheric ice crystals. The brightness temperature depressions previously alluded to in the sub-mm-wave spectral region will depend on assumptions about the particle size distribution, the shape and mass of the ice crystals, and their orientation with respect to an incident beam. It is known that the fractal nature of ice crystals follows particular power laws that describe their mass or density and area, and the mass of aggregating ice crystals generally follows mass–dimension relationships that are proportional to D^2, where D is the maximum dimension of the ice crystal [11–13]. There have been a number of attempts to construct idealised ice crystal models with specific mass–size relationships and apply these models to the development of databases of ice crystal optical properties in the microwave, and apply them to observations; see, for instance, the studies by Refs. [14–22]. The simulation of microwave brightness temperatures, between the frequencies of 10 and 183 GHz, using NWP-generated global model fields was found by Ref. [18] to be generally better using the sector snowflake model of Ref. [14] than by the assumption of soft ice spheres. The reason for this more generally improved simulation of observed brightness temperatures by a snowflake model was shown by Ref. [19] to be that it was an "average" representation of all other ice optical properties that they considered for the same mass of ice; they also found similar favourable behaviour for the eight-branched hexagonal ice aggregate model of Ref. [15], which was originally developed by Ref. [23]. Moreover, the assumption of the soft ice sphere was found not to be generally consistent at all of the frequencies considered by Ref. [19]. This "averaged" bulk optical property behaviour by a single shape of snowflake or ice aggregate might be sufficient to apply to frequencies in the microwave and sub-millimetre spectral regions to retrieve the IWP and bulk ice crystal size. However, previous studies that have assumed the eight-branched hexagonal aggregate have shown that the model generally over-predicts in-situ estimates of IWC by factors of about 2 [24]. This is because this model predicts a mass–dimension relationship that is proportional to D^3 and not D^2.

The same study concluded that it is better to assume a shape distribution of ice crystals to predict in-situ estimates of IWC. This was achieved by weighting each of the various members of the shape distribution at each size bin of the PSD, such that the observed IWC was reproduced to well within a factor of 2. In that study, it was necessary to apply such a weighting at each size bin owing to each particle model mass being proportional to D^3, but each model had differing pre-factor values in its mass-dimension relationship. Therefore, the shape distribution of idealised model particles could be made to behave as if their integrated mass values were produced by particles with mass being proportional to D^2. The sector snowflake model of Ref. [14] predicts a density–D relationship of the following form: $\rho \sim D^{-3/2}$, which implies a mass–D relationship also of the form $\sim D^{3/2}$. However, as stated earlier, current microphysical observations of ice aggregation and theory suggest that the mass of aggregating ice crystals should be proportional to D^2, which implies a density–D relationship of the form $D^{-1.0}$. The sector snowflake model of Ref. [14], with such a density profile, at large D values, will predict very low-density particles, as they will become very thin at those D values, relative to density models that predict a $D^{-1.0}$ relationship. These very low-density particles will become weakly interactive with microwave emission from the lower atmosphere and, as a consequence of being very low-density, they will become weakly interacting large particles, or WILPs for short. Thus, in the tropics, where very large D particles can occur, the sector snowflake model will be expected to predict microwave and sub-millimetre brightness temperatures that will probably be too warm relative to observation.

An alternative to simulating microwave scattering by single ice crystal models, soft spheres or soft spheroids is to assume an ensemble model of cirrus ice crystals. To this end, Ref. [25] developed the ensemble model of cirrus ice crystals. This model, which is shown in Fig. 1 in Ref. [25], consists of six shapes, which are a hexagonal ice column of an assumed aspect ratio, AR, of unity (i.e. the ratio of hexagonal column length to diameter), the six-branched bullet rosette, and then hexagonal monomers are randomly attached to build four ice aggregate models, which consist

of three-, five-, eight- and, finally, ten-branched hexagonal ice aggregates. The latter aggregate

models can cover the largest ice crystal sizes found in the particle size distribution (PSD), whilst the

former members can populate the smaller end of the ice crystal PSD. Alternatively, weights can be

assigned to each member of the ensemble model at each PSD bin size to compute the bulk ice

optical properties and/or the total mass of ice contained in the PSD, similar to Ref. [24]. The

applicability of the ensemble model in simulating observations of cirrus from across the spectrum

from different types of ice cloud in the mid-latitudes has been previously demonstrated by Ref.

[17]. In that reference, it is shown that by combining the ensemble model with a representative

moment estimation parameterisation of the PSD, as developed by Ref. [26], observations obtained

in the visible, infrared, microwave and radar regions of the spectrum could be simulated to good

accuracy. The ensemble model's predicted bulk ice optical properties have also been validated by

global observations of cirrus obtained at visible and infrared wavelengths [27, 28].

In this paper, we consider the two most extreme members of the ensemble model of cirrus ice

crystals, the first and sixth members only, which are the hexagonal ice column of aspect ratio unity

and the ten-branched hexagonal column aggregate. Hereinafter, to simplify the wording, the terms

"branched" and "hexagonal" are dropped so that each of the assumed aggregate models is described

more simply, owing to all models being composed of hexagonal ice crystals. For example, the latter

model is described as the ten-column aggregate. The bulk single-scattering properties of these two

models are computed using the light-scattering methods described in Part I. In Part I, it was shown

that the physical optics method was applicable in the microwave region down to size parameters of

about 18, where the size parameter was defined as $\pi D/\lambda$; this same definition of the size parameter

is used in this paper [29]. The bridging between the electromagnetic and physical optics methods

applied at size parameters smaller or greater than 18, respectively, was achieved using the ray

tracing with diffraction on facets (RTDF) method developed by Ref. [30]. It was argued in Part I

that the applicability of RTDF down to such low size parameters in the microwave region was

possible, owing to treating diffraction at each of the facets on the ray-tracing paths in addition to diffraction at the projected cross-section of the model ice crystal. Furthermore, the real refractive indices of atmospheric ice in the microwave are generally about 1.77; with such a large real refractive index, the processes of scattering are dominated by diffraction and reflection, both of which are treated accurately by RTDF. In principle, other physical optics methods could also be utilised in the microwave region in the same way as that shown in Part I, such as the methods developed by Refs. [31–33]. By replacing all electromagnetic solutions at a size parameter of 18 or greater with RTDF solutions, it was shown in Part I that the bulk integral ice optical properties of hexagonal columns of aspect ratio unity and eight-column aggregates could be replicated using the approximate solutions to generally within < 5% of the full electromagnetic solutions in the microwave. The scattering phase functions of the smooth hexagonal column and eight-column aggregate were also shown to be generally well replicated by RTDF at 243 and 874 GHz. This was also found to be the case for the bulk scattering phase function of the eight-column aggregate, where the latter was achieved by replacing, as above, electromagnetic solutions with RTDF solutions at size parameters of about 18 or greater at 874 GHz.

The electromagnetic results obtained from the eight-column aggregate used in Part I were extracted from the microwave single-scattering database compiled by Ref. [21]. The single-scattering databases described in Ref. [21] assume other randomly oriented model ice crystals, such as the ten-plate aggregate, five-plate aggregate, and the six-branched hollow bullet rosette, among others. The single-scattering results obtained for each of these randomly oriented model ice crystals were obtained using the methods of the Imbedded T-matrix and improved geometric optics [34, 35]. As discussed in Part I, the microwave database of Ref. [21] overcomes the difficulties of previous databases discussed above, as it considers a much greater range in atmospheric temperature, frequency, and a greater range in ice crystal maximum dimensions, out to 1cm-sized ice crystals. A further ice aggregate model that is considered here is the Voronoi particle model

developed by Ref. [36]. This model is based on the Voronoi tessellation of tiled polygons but realised in three-dimensional space to form a chain of polyhedral particles. A figure of the Voronoi model can be seen in Fig. 3 in Ref. [36].

In this paper, Part II, the bulk single-scattering solutions obtained for the model particles described above obtained from Ref. [21] are compared with those obtained for the two most extreme members of the ensemble model and the Voronoi model between the frequencies of 89 and 874 GHz. The purpose of this paper is to ascertain whether the bulk single-scattering properties of other ice aggregate models, calculated using state-of-the-art light scattering methods from Ref. [21], are generally bounded by the two most extreme members of the ensemble model, and the Voronoi particle. If so, this three-component model of ice cloud (i.e. the hexagonal ice column, eight-column aggregate and the Voronoi model) could generally be applied to microwave observations, rather than applying ice cloud models consisting of n combinations of various idealised ice crystals. Later on in the paper, the members of this three-component model will sometimes be referred to as members one to three, respectively. The applicability of this three-component model to forward model microwave observations obtained from a number of ice cloud cases will be the subject of the Part III paper.

The ISMAR instrument, as pointed out in Ref. [2], has frequencies located between 118 and 874 GHz and can be installed on board the Facility for Airborne Atmospheric Measurements (FAAM) aircraft [www.faam.ac.uk]. The 874 GHz channel will be added to ISMAR at some point during the summer of 2017. In this paper, we also consider frequencies relevant to the ICI instrument, which spans the range between 183 and 664 GHz. A further microwave instrument on board the FAAM aircraft is the Microwave Airborne Radiometer Scanning System (MARSS), which has channels located between 89 and 183 GHz. It is often the case that both ISMAR and MARSS are on board the FAMM aircraft at the same time. As mentioned in Part I, and as discussed in Ref. [2], the ISMAR instrument also measures vertically and horizontally polarised radiances; for

this reason, in this paper, the most relevant scattering matrix elements between the different ice crystal aggregate models are compared.

The paper is split into the following sections. In Section 2, the methodology of calculating the single-scattering properties of the two most extreme members of the ensemble model, the Voronoi model, assumed refractive indices, PSDs, and scattering definitions are defined. In Section 3, the bulk integral optical properties calculated for the various ice crystal models described above, obtained from the ice crystal model database of Ref. [21], are compared and contrasted with those calculated from the three-component model at frequencies between 89 and 874 GHz. Section 4 repeats this analysis for the most relevant bulk scattering matrix elements. In Section 5, differences between the various models are explored in brightness temperature space at frequencies of 183 and 874 GHz. In Section 6, the implications for single-scattering databases, in the microwave and sub-millimetre spectral regions, of observed ice crystal size spectra that significantly exceed ice crystal maximum dimensions of 1 cm are discussed. Finally, the salient points found in this paper, Part II, are summarised and discussed in Section 7.

2. Methodology and definitions

The randomly oriented bulk single-scattering properties of the two most extreme members of the ensemble model are calculated at frequencies between 89 and 874 GHz using the light-scattering methods of Monte Carlo ray tracing and the T-matrix developed by Refs. [39–41]. As in Part I, the electromagnetic methods are applied up to size parameters of about 18 at all frequencies considered. At size parameters greater than about 18, the Monte Carlo ray-tracing method of Ref. [39] is applied. In applying the Monte Carlo ray-tracing method, the two ensemble model members are randomised using the distortion parameter defined in Ref. [39]. The distortion parameter randomly tilts the facets of each of the model ice crystals with respect to its surface normal at each reflection and refraction event, thereby randomising the ray paths within the ice crystal model. This randomising process of ray paths within the ice crystal model results in featureless scattering matrix

elements as a function of the scattering angle, thus smoothing out optical features such as halos and ice bows. This randomising of each of the models is supposed to represent large-scale complexity of real ice crystals, where large-scale complexity is defined in Ref. [42]. By large-scale complexity we mean that ice crystals may be constructed from many ice crystal monomers of varying shapes and aspect ratios that are arbitrarily attached to form complex ice aggregates. Here, and in the calculations that follow, distortion values of 0.6 are applied to the two ensemble model members to represent very complex ice particles that ISMAR and ICI might sample. In Part I, the RTDF method developed by Ref. [30] was preferred over the ray-tracing method of Ref. [39], the latter of which considers only diffraction at the projected cross-section of the particle. However, in this paper we consider highly distorted ice crystals. With such large values of distortion parameters, there are insignificant differences between the calculated single-scattering properties using the two physical optics methods (not shown here for reasons of brevity). Therefore, for the purposes of this paper, the Monte Carlo ray-tracing method of Ref. [39] is considered sufficiently accurate.

The most extreme member of the ensemble model represents a complex ice aggregate, and to compute the single-scattering properties of this ice crystal requires electromagnetic methods other than the available T-matrix method of Ref. [40]. The T-matrix method of Ref. [40] is not applicable to the most extreme member of the ensemble model, as it is applicable to non-axisymmetric particles such as the finite hexagonal cylinder. Here, random orientation is considered, and owing to the analytic orientation averaging procedure available in the T-matrix, this makes it a more attractive method to apply than other methods such as the discrete dipole approximation (DDA) in terms of computational efficiency. To utilise the non-axisymmetric T-matrix method, we are therefore required to represent the ten-column aggregate ensemble model member through an approximate geometry at size parameters ≤ 18. As discussed in Ref. [17], the ensemble ten-column aggregate model considered in this paper is composed of hexagonal monomers that are well separated in space but are attached, meaning that multiple reflections between monomers that make

up the aggregate can be ignored. The meaning of this is that the phase function of one hexagonal monomer is similar to the phase function of the complete hexagonal ice aggregate owing to absorption, together with the inter-monomer reflections being weak. This behaviour in the phase function is seen even at visible wavelengths in Figs. 5 and 6 in Ref. [43], where it can be seen that the phase functions of the single component column or plate ice crystals are similar to spatial aggregates of these particles. Moreover, it has more generally been shown that the scattering matrix elements of complex ice crystals are similar to the scattering matrix elements of their single component ice crystals [44–46]. With absorption and distortions applied to the model particles, such differences will be even smaller, and these conditions will be met in the microwave. Therefore, based on the previous theoretical studies, we simplify, here, and hereinafter, the ice aggregate ensemble model member to calculate the single-scattering properties of this member by assuming equal area ratio hexagonal ice columns, thus preserving a microphysical property of this ensemble model member. The area ratio is defined as the ratio of the projected area of the orientation-averaged non-spherical ice crystal of size, D, to the projected area of the circumscribed circle of the same D.

It was previously shown in Ref. [47] that the area ratios predicted by the members of the ensemble model are well within the ranges of in-situ measured area ratios obtained from a number of field campaigns, which were located in Arctic, mid-latitude and tropical regions. Moreover, balloon-borne microphysical measurements of the area ratio of ice crystals obtained in high-latitude cirrus by Ref. [48] were found to be consistent with some ensemble model member predictions of the area ratio. For those cases in which the T-matrix method of Ref. [40] was found to be non-convergent, owing to large hexagonal ice column aspect ratios, the T-matrix method of Ref. [41] was applied to circular ice cylinders with the same area ratio as that of the ten-column aggregate model. In the case of the hexagonal ice column of aspect ratio unity, the simplification to circular ice cylinders was found to be unnecessary. At size parameters > 18, the Monte Carlo ray-tracing

method was applied to the actual geometry of the two ensemble model members without approximation. The simplification of the ten-column aggregate model to equal area ratio hexagonal ice columns and cylinders will be severely tested at the frequency of 89 GHz, as at that frequency size parameters > 18 are not considered.

In the case of the Voronoi model and as discussed in Ref. [36], this model can be constructed to follow any density–dimension relationship. In this paper, the model follows the density–dimension relationship derived in Ref. [37]. The latter derivation was based on in-situ airborne bulk measurements of IWC and estimates of IWC, where the estimates were based on a variety of microphysical probes, as obtained in a number of cold mid-latitude cirrus cases. They found from these in-situ measurements that the best mass–dimension relationship was found to have the following form: $m=0.0257D^2$, where m is the mass of aggregating ice and the units are in SI. This derived mass–dimension relationship implies an effective density, ρ_e, of the following form: $\rho_e=0.049D^{-1.0}$, where the effective density is given by the equivalent mass of an ice sphere of diameter D. Thus, the Voronoi model follows a generally observed effective density–size relationship.

The single-scattering properties of the Voronoi model have been calculated using a non-standard finite-difference time-domain method (FDTD), as used in Ref. [36] and applied to the global remote sensing of ice cloud in Ref. [28], and the discrete dipole approximation (DDSCAT) version 7.3 available via http://www.ddscat.org/ [38]. The FDTD method was applied at size parameters between 1 and 70, whilst the DDSCAT method was applied at size parameters greater than 70. For size parameters of less than 1, the DDSCAT method was applied owing to the difficulties of applying the FDTD method to very small particles. The DDSCAT method was applied to the Voronoi model at up to maximum ice crystal dimensions of 1.5 cm, between the frequencies of 10 and 874 GHz. An example of the input data used in the electromagnetic computations at 664 GHz can be seen in the Appendix to this paper. The DDSCAT electromagnetic computations were

performed on an HP Z-840 Workstation (CPU Intel Xeon 3.10 GHz) and the FDTD computations utilised an Intel-C compiler.

The assumed refractive indices of atmospheric ice applied here are the same as those used in Part I, and are taken from the compilation made available by Ref. [49]. The bulk scalar optical properties used here were previously described in Part I, and are given by Eqs. (3–6) in that paper, i.e. the orientation-averaged bulk extinction and scattering coefficients, β_{ext} and β_{sca}, respectively, the single-scattering albedo, ω_0, and the asymmetry parameter, g. The PSDs assumed in calculating the bulk integral ice optical properties were also described in Part I, in Section 3.3, and are shown in Fig. 5 in that paper. In Section 3.3 in Part I, the mean mass-weighted size, D_{mmw}, is given by Eq. (2), and exactly the same PSDs and values of D_{mmw} as those used in Part I are applied in this paper. As a reminder, the mean mass-weighted size is defined as the ratio between the third and second moments of the PSD, where the second moment is given by the mass of ice contained in the PSD. Hence, D_{mmw} is a mass-weighted characteristic size of the PSD. The values of D in the PSDs do not exceed 1 cm.

In some microwave, radar and sub-millimetre studies the characteristic ice crystal size of the PSD is usually given by the effective dimension, D_e, of the PSD. However, the definition of D_e is that of the ratio of the total mass of ice contained in the PSD to the orientation-averaged cross-section of the PSD [50]. In the case of aggregating ice crystals, as argued in Ref. [51], D_e will tend to near constant values, simply because the numerator, as discussed in Section 1, becomes proportional to D^2 and the denominator, in the case of the aggregating ice crystals observed in Ref. [12], becomes proportional to $D^{1.71-1.76}$. Therefore, D_e has a $D^{0.29-0.24}$ dependence on D, given the data supplied by Ref. [12]. Clearly, such a definition of characteristic ice crystal size of the PSD cannot be usefully applied to microwave, radar and sub-millimetre observations, as D_e will become weakly dependent on IWC. Therefore, the definition of D_{mmw} is preferred, since D_{mmw} is weighted by the mass of ice, and it is the mass of ice that is directly proportional to the brightness

13

temperature depressions observed at microwave frequencies previously discussed in Section 1.

Given the methodology and definitions defined in this section, in the next section the bulk integral optical properties calculated for the three-component model are compared and contrasted with the other ice crystal models previously discussed in Section 1 at frequencies between 89 and 874 GHz. The frequencies represent the range in central frequencies available on the ICI, MARSS and ISMAR instruments. In the next section, we compare bulk integrated optical properties rather than single-scattering properties as a function of D, as in reality, ice clouds are polydispersive in size and individual ice crystal interference effects are averaged out, once integrated over the PSD as demonstrated by Ref. [52]. In that paper, it was concluded that removing interference effects through the integration of the single-scattering properties over PSDs provides a more natural simulation of the optical properties of non-spherical particles. Moreover, here we wish to demonstrate that in the microwave, the choice of shape of the PSD might be as important as choice of ice crystal shape.

3. Comparisons of the bulk integral ice optical properties in the microwave region

The three-component model integral ice optical properties have been calculated at an assumed temperature of about 240 K. The microwave single-scattering properties made available by Ref. [21] were calculated at the temperature values of 160, 200, 230 and 270 K using atmospheric ice refractive indices compiled by Ref. [53]. It is known that the imaginary part of the ice refractive index in the microwave region is temperature-dependent, as discussed in Refs. [21, 54]. The integral optical properties of the ice particle models are compared using the databases computed at the temperatures of 240 and 230 K. However, absolute differences in the real and imaginary refractive indices between the two compilations, at these two temperatures and at the two most extreme frequencies of 89 and 874 GHz, are about 1% and less than 1%, respectively. Such small absolute differences between the two refractive indices at the two temperatures are not considered

significant, for the purposes of this paper. The geometry of the ten- and five-plate aggregates, eight-column aggregate, and six-branched hollow bullet rosette is detailed in Ref. [55].

Firstly, the bulk extinction coefficient is compared between the different ice crystal models as a function of D_{mmw}, the results of which are presented in Fig. 1 at the frequencies of 89 and 243 GHz, and in Fig. 2 at the frequencies of 325 and 874 GHz. The results presented in Fig. 1 show that the three-component model, at the lower frequencies of 89 and 243 GHz, do indeed generally bound the other ice aggregate models at all D_{mmw} values considered. The most notable exception to this is the non-aggregated six-branched hollow bullet rosette, where its bulk extinction coefficient values are generally smaller than that predicted by the most extreme member of the three-component model at 89 GHz for 50 μm $< D_{mmw} <$ 2000 μm, and this same behaviour is also seen at the frequency of 243 GHz for $D_{mmw} <$ 1000 μm. We note here that the ten-plate aggregate model also, at some values of D_{mmw}, has lower bulk extinction values than the third member of the three-component model for $D_{mmw} <$ 200 μm at the two frequencies shown in Fig. 1. However, these latter values of D_{mmw} near 100 μm or less will probably not be important in the microwave. It should also be noted here that at the smallest value of D_{mmw} shown in Fig. 1, the third member of the three-component model is roughly an average of the first two members of this model. This is because at the smallest D_{mmw} values, the Voronoi model behaves more as a solid particle, where the mass is proportional to D^3. Moreover, note also that the eight-column aggregate volume extinction coefficient is greater than that of the other ice aggregate models, owing to this model being compact rather than chain-like. The results of comparing the extinction coefficients predicted by the various models at two sub-millimetre frequencies can be inspected in Fig. 2.

Fig. 1. The bulk extinction coefficient plotted against the mean mass-weighted size, D_{mmw}, at the frequencies of 89 (top panel) and 243 GHz (bottom panel). The key to each of the ice crystal models is shown in the top-left in each of the panels. The three members of the three-component model are shown in the key as Mem 1 (i.e. the hexagonal ice column of AR=1), Mem 2 (i.e. the ten-column aggregate), and Mem 3 (i.e. the Voronoi model).

It can be seen from Fig. 2 that similar behaviour between the differing ice models is observed,

as shown in Fig. 1, that is the three-component model generally bounds the other ice aggregate

models, with the exception of the non-aggregated six-branched hollow bullet-rosette. However, at the highest frequency of 874 GHz, the first two members of the three-component model generally bound all other ice aggregate models for all values of D_{mmw} considered, with the six-branched hollow bullet rosette and ten-plate aggregate sometimes exhibiting bulk extinction coefficient values lower than any member of the three-component model at some values and at one value of D_{mmw}, respectively. At the lower sub-millimetre frequency, the first and third members of the three-component model predict a bulk extinction which generally bound all other aggregate models. The six-branched hollow bullet rosette predictions of the bulk extinction coefficient show similar behaviour to that in Fig. 1, i.e. this model tends to be the most divergent from all of the other models. However, the Voronoi model (member 3 of the three-component model) has been constructed so as to have an effective density–D profile similar to an observed power law. Thus, this particle behaves more like a hollow particle as its effective density decreases with increasing D; this is especially the case as the imaginary index of ice decreases at the lower frequencies considered in Figs. 1 and 2.

A further important point to draw from Figs. 1–2 is that the values of the bulk extinction coefficients can be quite different from nearest-neighbour D_{mmw} values for the same ice crystal model. This is because, as shown in Fig. 5 in Part I, the shapes of the PSDs are quite different as a function of D. Even though similar values of D_{mmw} can be obtained from PSDs of different shapes, this can result in quite different values for each of the bulk extinction coefficients, even with similar D_{mmw} values. Therefore, the assumed shapes of the PSD are just as important as the assumed ice crystal model shapes when interpreting mm-wave and sub-mm-wave observations. This point was also noted in Ref. [18].

Fig. 2. The same as Fig. 1 but for the frequencies at 325 (top panel) and 874 GHz (bottom panel).

In the figures that follow, the results of comparing the co-albedo (i.e. $1-\omega_0$) between the different ice crystal models are presented in Figs. 3–4. As before, in Fig. 3, results for 89 and 243 GHz are presented, whilst in Fig. 4, results are shown for 325 and 874 GHz. At the least ice-absorbing frequency shown in the figure, at 89 GHz, the third member of the three-component model and six-branched bullet rosette models are the most absorbing relative to all other models for all values of D_{mmw} considered. This being also generally true at 243 GHz, except for $D \gg 1000$ µm, when the first member of the three-component model becomes the most absorbing relative to all other models. This behaviour of the third member of the three-component model is because the other models are chains of hexagonal columns and plates; therefore, these tend to scatter more between the individual monomers that make up each of the other particle models, thus resulting in less absorption. Contrary to Fig. 1, at the lowest frequency, the eight-column aggregate, owing to this model being more compact rather than chain-like, scatters more radiation than do the other ice aggregate models at the same values of D_{mmw}. At 89 GHz, the second member of the three-component model generally scatters similarly to the five-plate aggregate. However, at 243 GHz, the ten-plate aggregate model scatters more radiation generally than do the other ice particle models shown in the figure, whilst the eight-column aggregate model scatters radiation similarly to the second member of the three-component model. At 89 GHz, the ten-plate aggregate model is generally more absorbing than the second member of the three-component model at all values of D_{mmw} considered.

Fig. 3. The co-albedo (1.-w0), plotted as a function of D_{mmw} at the frequencies of 89 GHz (top panel) and 243 GHz (bottom panel). The key to each of the ice crystal models is shown in the top-right in each of the panels and is the same as shown in Fig. 1.

The co-albedo comparisons at the two sub-millimetre frequencies are presented in Fig. 4. At the most ice-absorbing frequency of 874 GHz, and at D_{mmw} values greater than about 400 μm, the third member of the three-component model becomes less absorbing relative to the other models, simply

because this model has less ice mass with which to absorb the incident microwave radiation; this behaviour is most apparent when $D_{mmw} > 1000$ μm. For $D_{mmw} > 400$ μm, the three-component model bound all other ice models considered. At D_{mmw} values less than about 400 μm, the three-component model bound the five-plate and eight-column ice aggregates, with the ten-plate aggregate and six-branched bullet rosette being somewhat more scattering than the three-component model at some values of D_{mmw} less than about 400 μm. At 325 GHz, the ten-plate model generally absorbs the least compared to the other ice particle models, whilst the eight-column aggregate is generally bounded by the first two members of the three-component model. Moreover, at this frequency, when $D_{mmw} < 300$ μm, the third member of the three-component model becomes much more absorbing than all other models.

Figures 3–4 show that at the least ice-absorbing frequency of 89 GHz, as expected, particles with the least amount of ice mass become generally the more absorbing. On the contrary, at the most ice-absorbing frequency of 874 GHz, these same ice particle models become the least absorbing, owing to the other particle models containing more ice mass. As discussed in Section 1, the eight-column aggregate model has more ice mass than do the more chain-like models, as represented by the ten- and five-plate, and the ten-column aggregate models, but it is also more compact. As a result of these properties, the model scatters radiation the most of all of the models at 89 GHz, but at 874 GHz, the model will be significantly more absorbing than the other ice aggregate models. Moreover, as already shown in Figs. 1–2, the shape of the assumed PSDs is important in determining the bulk absorption properties of each of the ice crystal models. For example, at around the nearest-neighbour D_{mmw} values of about 200 and 400 μm, the absorption properties of the model ice particles can be quite different but with similar D_{mmw} values. We emphasise here that choice of PSD shape is as important as ice crystal model selection. This is why in this section it is more important to contrast the bulk integral optical properties rather than their

single-scattering counterparts as a function of D.

Fig. 4. The same as Fig. 3 but for the frequencies at 325 GHz (top panel) and 874 GHz (bottom panel).

As can be seen by an examination of Figs. 1–2, if the first member of the three-component model were to be ignored, relative to the various chain-like aggregates and low ice mass models, the eight-column aggregate model would predict bulk extinction coefficient values much greater

than those of other models, and as such, no longer in this space represents an "average" behaviour of all possible aggregated models that could be considered. This is why it is important to consider other models with actual hollowness and models which follow generally observed effective density–size relationships. Hence our inclusion of the Voronoi model as the third member of the three-component model, as this helps to represent potentially more realistic particles when simulating microwave observations. In Section 5, the properties shown in Figs. 1–4 are applied to a radiative transfer model to understand how the differing ice crystal models behave in brightness temperature space as a function of D_{mmw}.

4. Comparisons of the scattering matrix elements at 89 and 874 GHz

Here, the more relevant scattering matrix elements of the randomly oriented members of the three-component model are compared with the same scattering matrix elements predicted by the other randomly oriented ice particle models discussed in Section 3. The elements of the scattering matrix of randomly oriented ice particles that possess planes of symmetry have been previously defined and discussed in Ref. [41]. As discussed in Ref. [41], for randomly oriented particles with planes of symmetry, there are six independent elements of the scattering matrix: P_{11}, P_{12}, P_{22}, P_{33}, P_{43} and P_{44}. However, the ISMAR and ICI instruments measure the linear polarisation and not the circular polarisation, since there are no coherent sources of circular polarisation in the atmosphere; therefore, the circular polarisation elements (i.e. P_{43} and P_{44}) are not included in the comparisons as these will not contribute to the linear polarisation measurements obtained using the ISMAR and ICI instruments. Moreover, for the case of random orientation, the P_{11} and P_{22} elements are very similar to each other, and so for this reason, we do not present results for the P_{22} element.

The P_{11}, P_{12}, P_{33} elements predicted by the three-component model are calculated, using the methodology discussed in Sections 1 and 2, at the lowest and highest frequencies of 89 and 874 GHz that were considered in Section 3. These two frequencies have been selected so as to contrast results at a low and moderate size parameter. The scattering matrix elements predicted by the

various ice particle models are compared at the same temperature values given in the previous section. Rather than present results at each ice crystal maximum dimension, here, an arithmetic average of each of the scattering matrix elements is presented at each frequency. The arithmetic average is obtained over the following five ice crystal maximum dimensions: 100, 500, 1000, 3500 and 10,000 μm. These chosen maximum dimensions cover the range of ice crystal sizes that will be important in mm-wave and sub-mm-wave remote sensing, especially the latter values. As a result of this average maximum dimension, the average size parameters at 89 and 874 GHz are 2.8 and 27.7, respectively.

Firstly, the results of comparisons at 89 GHz are presented in Fig. 5. In each of the figures, where appropriate, the results are presented as the common logarithm of the scattering matrix elements, so that differences between each of the ice particle models can be more easily seen. In the case of the P_{33} element, each of these elements is normalised by the P_{11} element so that differences between models can be more easily ascertained.

Fig. 5. The 89 GHz scattering matrix elements calculated for each model are plotted against the scattering angle. The key to each of the ice particle models is shown in each of the panels. The first element $\log_{10}(P_{11})$ is shown in the top panel, together with each models asymmetry parameter. The P_{12} element is shown in the middle panel, and the P_{33}/P_{11} is shown in the bottom panel.

The asymmetry parameter values alongside each of the ice particle models presented in Fig. 5 (top panel) have been calculated directly from each of the scattering phase functions by using the definition of the asymmetry parameter given in Ref. [40]. In the figure, the three models comprising the three-component model (i.e. Mem 1, Mem 2 and Mem 3) are shown as the two full lines and the dashed line, coloured in black, red and grey, respectively. The results have been plotted in this way to show more easily if the three-component model bound the other ice particle models. Firstly, at the frequency of 89 GHz, the second member of the three-component model is represented by the equal area ratio hexagonal ice column as discussed in Section 2. This approximation does not appear to be markedly detrimental, as shown in the figure. Indeed, the three-component model does generally bound most of the other ice crystal models. The exception to this is the six-branched hollow bullet rosette, however, this model behaves similarly to the third member of the three-component model. This is similar to the results shown in Section 3. This is particularly seen to be the case for the P_{12} element, where the six-branched hollow bullet rosette and Mem 3 appear to be similar but have more negative values than do all of the other ice crystal models, and at around the scattering angle of 80°, the six-branched hollow bullet rosette is slightly more negative than Mem 3. Thus, at 89 GHz, the three-component model does generally bound all other ice aggregate models shown in the figure.

This is also true for the phase functions predicted by the three-component model members, as they also do generally bound the other ice aggregate models at most of the scattering angles shown. At scattering angles greater than about 100°, all ice models scatter similarly with the exception of Mem 1. Indeed, the asymmetry parameter values calculated from each of the first two members of the three-component model phase functions are the highest and lowest of all of the asymmetry parameter values shown in the figure. This same bounding of the other ice aggregate models by the three-component model members is also generally true for the P_{33}/P_{11} scattering matrix element, where in this case, the six-branched hollow bullet rosette and Mem 3 behave similarly at all

scattering angles.

The results of comparing the selected scattering matrix elements of the ice particle models calculated at the frequency of 874 GHz are shown in Fig. 6. At this frequency of 874 GHz, the first two members of the three-component model are shown to generally bound the phase functions of all other ice particle models at most of the scattering angles. The asymmetry parameter values calculated from each of these two members are the highest and lowest of all of the asymmetry parameter values shown in Fig. 6, a finding similar to Fig. 5. Results shown for the P_{12} element indicate that the second and third members of the three-component model have linear polarisations similar to each other. At low scattering angles, less than about 30°, the other more regular models (in the sense that no distortion values have been applied to the other models) are most different from each other and the members of the three-component model. If these other ice particles were randomly distorted, it is expected that they would behave similarly to the three-component model. The other point to note from Fig. 6 is that the other chain-like ice aggregate models, at scattering angles greater than about 30°, also behave similarly to the second and third members of the three-component model. This finding is consistent with the ray-tracing calculations presented in Part I for the P_{12} element, which suggested that there might be a limit to discriminating ice crystal complexity using linearly polarised observations. On the other hand, the eight-column aggregate P_{12} values are most different from those of the chain-like ice models; therefore, this result may indicate that there is information on discriminating between compact and chain-like ice aggregates in the sub-millimetre. If the particles were purely horizontally oriented, then it would be expected that these noted differences would become more pronounced according to the linear polarisation studies presented in Ref. [56]. However, even in random orientation, polarisation differences in the sub-mm are dependent on assumed ice crystal shape as shown in Ref. [21].

Fig. 6. The same as Fig. 5 except for 874 GHz.

At 874 GHz, in the case of the P_{33}/P_{11} element results presented for the second member of the three-component model have been calculated assuming the equal area ratio circular ice cylinder to see, similarly to Fig. 5, if this approximation can be used to represent complex ice crystals in the lower order scattering matrix elements. Again, the three-component model members are shown to generally bound all other ice aggregate model results at most of the scattering angles shown. The exception to this, once again, is the six-branched bullet-rosette, which has slightly lower values of P_{33}/P_{11} than the second member of the three-component model between the scattering angles of about 80° and 130°.   Interestingly, in the P_{33}/P_{11}, we note that the eight-column aggregate at scattering angles greater than about 100° becomes more divergent from the other ice models and tends to the first member of the three-component model.

In this section and in the previous section, the three-component model has been shown to, indeed, generally bound the other ice aggregate particle models considered in this paper, especially in the sub-mm-wave spectral region. The model that has been shown to be most divergent from other models is the six-branched hollow bullet rosette. However, in some of the cases presented, this model behaves similarly to the third member of the three-component model. This result shows the need to consider particles which are actually hollow and/or particles which closely follow observed density–D power laws in the microwave region.

5. Brightness temperature differences between differing ice crystal models at 183 and 874 GHz

Here, brightness temperature differences are obtained between the second member of the three-component model and the other ice particle models at 183 and 874 GHz. This model is chosen as it can represent an "average" of the bulk extinction results shown in Section 3 at the lower frequencies, and at the highest frequency of 874 GHz, it can have one of the lowest volume extinction values of all the other models shown. The frequency of 183 GHz is chosen because this represents the highest central frequency that is currently available on board Earth observation

satellites. The frequency of 874 GHz is the highest central frequency available on the ISMAR instrument. Differences between the ice models at these two frequencies will indicate which values of D_{mmw} are the more likely to be sensitive to significant deviations in brightness temperature between different assumed ice models. The radiative transfer model used in this section to obtain the various brightness temperature differences is the same delta-Eddington two-stream approximation used in Section 4 in Part I; therefore, a description of the model will not be repeated here. However, in this paper the standard mid-latitude summer atmosphere is assumed and the cirrus of an assumed geometrical vertical depth of 3 km is located at an altitude of 10 km. The surface and cloud temperature values are assumed to be 294.20 and 235.3 K, respectively. Note that the cloud temperature is similar to the temperature assumed in all of the other sections of this paper to calculate the bulk single-scattering properties. The accuracy of the radiative transfer model has also been previously discussed in Section 4 in Part I and was considered sufficiently accurate for the purposes of sensitivity studies. The required inputs into the delta-Eddington two-stream approximation are the integral optical properties discussed in Sections 3 and 4, which are the extinction coefficient, single-scattering albedo, and the asymmetry parameter. The differences noted between the various ice crystal models in the previous sections are now explored in brightness temperature space.

To examine the brightness temperature differences, the brightness temperatures calculated while assuming the second member of the three-component model, hereinafter referred to as the "control", are subtracted from all of the other ice crystal models. The results of these calculations at 183 and 874 GHz are shown in Fig. 7.

Fig. 7. Brightness temperature differences (BT diff K) obtained between the control and all other ice crystal models plotted against D_{mmw} at 183 GHz (top panel) and 874 GHz (bottom panel). The key to each of the brightness temperature differences are shown in the top-left and bottom-left in each of the panels, respectively.

The figure shows that at 183 GHz, brightness temperature differences between the control and

the other ice crystal models do not exceed values greater than about 10 K until $D_{mmw} > 400$ μm. Thereafter, brightness temperature differences become well separated between this model and the eight-column aggregate model at most of the D_{mmw} values shown in the figure. Interestingly, at 183 GHz, differences between the control and the five-plate aggregate stay generally well within brightness temperature differences of about 10 K for all values of D_{mmw} considered. The ten- plate aggregate, and hollow bullet rosette particle models become significantly different from the control when D_{mmw} values exceed about 600 μm, i.e. greater than about -20 K. However, at this frequency, the brightness temperature differences shown do not compete with other brightness temperature differences on the order of 40 K that can be found in the literature, owing to uncertainties in microphysics until $D_{mmw} > 1000$ μm [57].

The greatest brightness temperature differences between the control and the other ice crystal models are induced by the third member of the three-component model and the six-branched hollow bullet rosette, and these differences can be of the same order as that found for differences resulting from the uncertainties in cirrus microphysics [57]. However, the differences between these two models and the control are similar. Therefore, it would be expected that, at least at this frequency, the three-component model should encompass most of the observed brightness temperatures. At the traditionally highest Earth-observing microwave central frequency, differences between differing ice particle models become most apparent only at the largest values of D_{mmw} considered in this paper. Another interesting feature at 183 GHz is that brightness temperature differences between the control and the eight-column aggregate are positive, while for other ice particle models they are negative. The physical reason for this is as follows. As shown in Section 3, the eight-column aggregate model has a significantly greater bulk extinction coefficient than that of the control model considered in this section, thus resulting in less upwelling microwave radiation relative to the control; consequently, positive brightness temperature differences are induced. On the other hand, as also shown in Section 3, the hollow bullet rosette and third model member of the

three-component model have the smallest bulk extinction values at this frequency. Indeed, in Fig. 1 at the largest D_{mmw} values the bulk extinction coefficients of the most control and the hollow bullet rosette and third model member differ by more than one order of magnitude therefore, in these cases, the brightness temperature differences become negative between the control and these two ice crystal models resulting in differences of over 100 K at the largest values of D_{mmw}.

As Fig. 7 demonstrates, at the sub-mm-wave frequency of 874 GHz, there is more sensitivity to assumed ice crystal shapes than at 183 GHz. At this higher frequency, significant brightness temperature differences greater than ±5 K occur between the control and some of the other ice particle models when 100 μm ≤ D_{mmw} < 400 μm. The previous statement is, however, only true for the eight-column aggregate and third member of the three-component model. Brightness temperature differences between the control and all other models exceeding ±5 K do not occur until D_{mmw} > 400 μm. At the higher sub-mm-wave frequencies on board ISMAR and ICI, the brightness temperature deviations observed here should be sufficient to enable discrimination between some of the models considered in this paper at moderate values of D_{mmw}, and such values might be typically encountered in mid-latitude ice cloud. The greatest brightness temperature differences between the control and the other ice particle models are, once again, observed at the largest values of D_{mmw}, and such values should be readily detected in the tropics or in convective ice cloud. Interestingly, the third member of the three-component model generally induces positive brightness temperature differences relative to the control, owing to this third member predicting greater values of the bulk extinction coefficient than the control shown in Section 3. For D_{mmw} > 400 μm, the other ice particle model members generally induce negative brightness temperature differences relative to the control. This is because at this frequency, with increased ice absorption (owing to the larger ice imaginary index at this frequency), the backscattered fraction (i.e. approximately 1 - $\omega_0 g$) of incident microwave radiation is greater for the control than for the other ice particle models

considered here, thereby inducing the negative brightness temperature differences.

Also noteworthy at the frequency of 874 GHz is the behaviour in the brightness temperature differences at D_{mmw} values that are close to each other, owing to the differing shapes of the PSD, as previously discussed in Section 3. This is particularly apparent at around D_{mmw} values near about 450 μm; note that at that D_{mmw} value, brightness temperature differences can change by more than about 30 K for the six-branched hollow bullet rosette and ten-plate aggregate. In Ref. [21], the importance of the ice crystal shape to the retrieval of the particle size and IWP was emphasised at microwave frequencies. Here, we reiterate the importance not only of the assumed ice crystal shape but also of the adopted shape of the PSD. It is this latter aspect which is further explored in the next section.

6. The potential importance of observed very broad PSDs in the microwave region

The most recent ice crystal single-scattering databases have considered ice crystal maximum dimensions no greater than 1 cm. This is a considerable improvement upon previous databases which considered maximum dimensions less than this. In this section, we show why, for the purposes of global remote sensing of ice cloud properties in the microwave, ice crystal single-scattering databases should be constructed in which the maximum dimensions extend to 5 cm.

There are a few observations of PSDs which clearly show the significant occurrence of ice crystal maximum dimensions extending to 5 cm. One such study is presented in Ref. [58], where they show the occurrence of up to 5 cm snow aggregates near to the cloud base. These snow aggregates are postulated to be formed by the sedimentation of ice aggregates which, in turn, aggregate on snow grains to form cm-sized snow aggregates [58]. To date, PSD moment estimation parameterisations such as the one developed by Ref. [26] do not consider such broad PSDs; as such, observations were missing from the data used to construct the parameterisations. To demonstrate this point, the PSD parameterisation of Ref. [26] is compared to the measured PSDs taken from Ref. [58].

The moment estimation parameterisation of Ref. [26] is based on 10,000 in-situ measurements of the PSD and IWC, which were measured between the temperatures of 0°C and -60°C during a number of cirrus field campaigns located in the mid-latitudes and tropics. The parameterisation is based on the moments of the PSD, given by the integral product of D^n and f(D), where f(D) is the PSD, which gives the particle number concentration at each D, and n ≥ 0. Therefore, the zeroth moment (i.e. n = 0) is the total number concentration of particles per unit volume of cloudy air. The other moments of the PSD are related to the 2nd moment (M_2) (i.e. the mass-carrying moment if the mass of aggregating ice crystals is proportional to D^2) through a relationship of the form $M_n = \sigma_n M_2^{\beta_n}$, where σ_n and β_n are functions of in-cloud temperature, T_c. Therefore, given all M_n, the full PSD can be estimated from the IWC and T_c values via an assumed mass–D relationship. It was shown in Ref. [26] that no universal PSD could be found that described all of the in-situ PSDs obtained in the mid-latitudes and tropics. Therefore, normalisations had to be applied to the mid-latitude and tropical in-situ dataset to obtain separate parameterisations that can be applied in those two latitude regions.

The comparisons between the parameterised and observed PSDs discussed above are presented in Fig. 8. The observed PSDs were digitised from Ref. [58] using the digitisation tool available at http://arohatgi.info/WebPlotDigitizer/. This tool had to be used as the original data from the authors of Ref. [58] are no longer available. To generate the parameterised PSDs shown in Fig. 8, the IWC and T_c parameters were assigned the values of 1.7 gm^{-3} and $-1.8^{o}C$, respectively, which were estimated from near the cloud base of Ref. [58]. The figure shows that the two parameterisations do reproduce the observations at sizes less than about 1 cm. However, at sizes greater than this, the parameterisations fail to include ice aggregates greater than about 2 cm in size. After this size, the number concentrations in both PSD parameterisations exponentially fall off. However, this exponential decay is not observed in the case studies in Ref. [58], owing to the ice aggregates not

being removed from the cloud as might be expected; instead they aggregate on the snow grains to

form the observed cm-sized ice aggregates.
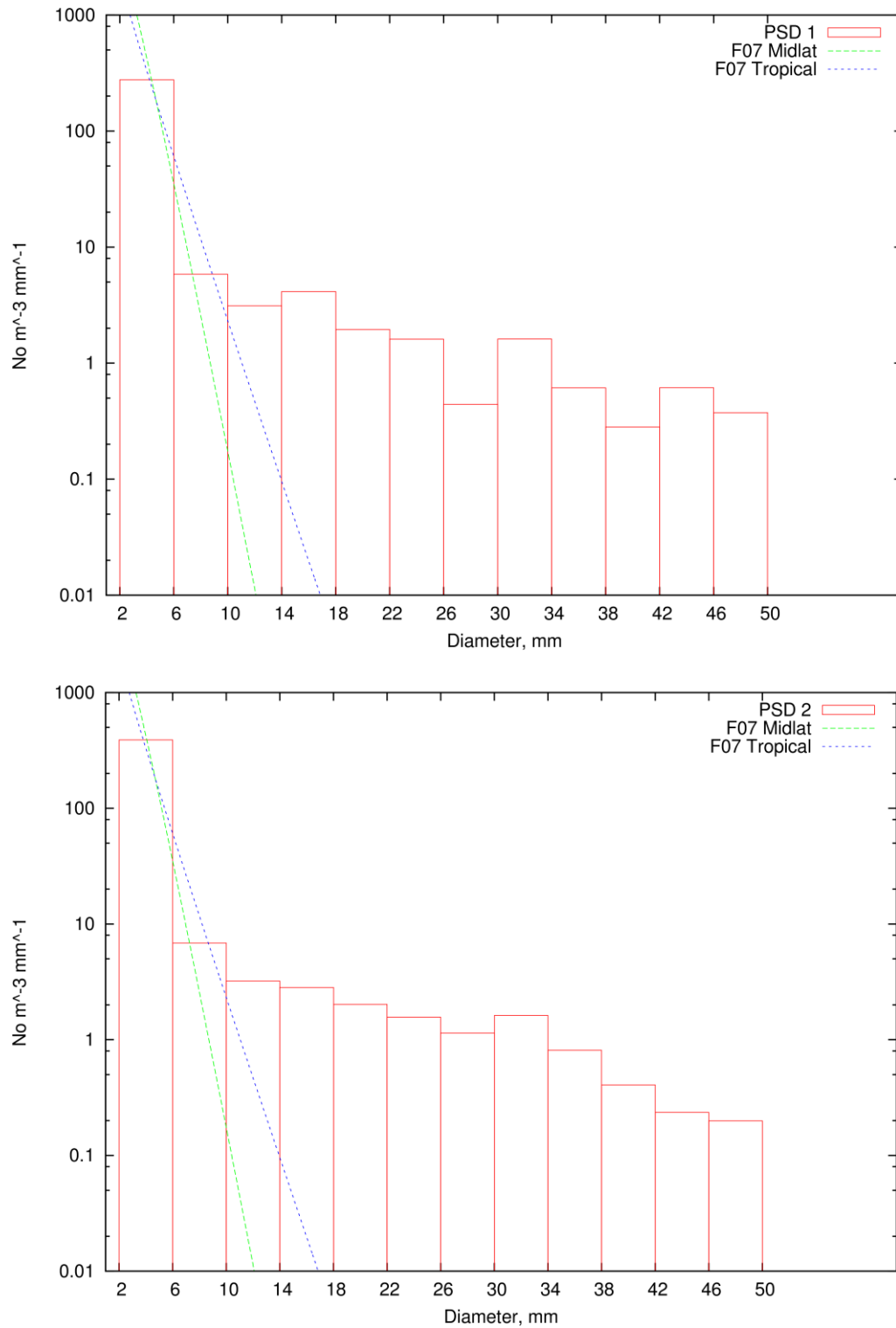

Fig. 8. Comparison between the parameterised moment estimation PSD from Ref. [26] (F07) and observed PSDs from Ref. [58]. The top and bottom panels show the observed PSDs obtained at differing times near the base of the cloud. The PSD parameterisations are represented in both panels by the mid-latitude (green dashed line) and tropical (blue dashed line) normalisations.

The figure highlights the problem with current PSD parameterisations, which are utilised in NWP and climate models: they do not include observations of very broad PSDs. Clearly, this situation needs to be remedied through the greater use of the microphysical instrument used in Ref. [58], which is capable of measuring cm-sized ice aggregates. The moment estimation parameterisation of Ref. [26] has been previously compared to in-situ PSDs measured in the mid-latitudes and tropics; however, these cases are few in number. In the case of the tropics, Ref. [59] found that the moment estimation scheme fit well with several cases of averaged in-situ measured tropical PSDs. For several cases of mid-latitude cirrus, Ref. [60] compared the estimated moments to in-situ measured moments, whilst ignoring particles less than 100 μm in size, owing to the current uncertainties in measuring the size of small ice at D < 100 μm, and they found good correlations between the parameterisation and measurements for all cases considered. However, poor correlations emerged in that study when the moments predicted by the parameterisation developed by Ref. [61] were compared with the in-situ derived moments.

It is now interesting to compare the derived integral optical properties using the two observed PSDs and the PSD parameterisation at the lowest and highest frequencies considered in this paper, at 89 and 874 GHz, assuming the control model used in the previous section. This model is used here as it is the only ice aggregate model for which the integral optical properties are available for maximum dimensions up to 5 cm. However, the control model is composed of ten monomer ice crystals, in reality the observed snow aggregates are likely to be composed of many more monomers than considered here. On the other hand, the integral optical properties ω_0 and g of spatial ice aggregates tend to asymptotic values after the addition of three monomer ice crystals as shown in Ref. [43]. We do not suppose this behaviour to be any different here. Moreover, the area ratios predicted by the control model are within in-situ experimental uncertainties of area ratios of fractal ice crystals as shown in Ref. [47]. In that paper, the area ratios are presented for fractal ice crystals of maximum dimensions up to 1 cm. However, the

projected area predicted by the control model are still within experimental uncertainties for crystal dimensions up to 5 cm using the area-dimension relationship derived from Ref. [12], not shown here for reasons of brevity. Therefore, we consider the results presented in this section to be of practical value in snow conditions in the calculation of bulk integral optical properties.

The results of these comparisons are shown in Tables 1 and 2. Table 3 shows comparisons between the backscattered fractions, bf, where bf ~ $(1 - \omega_0 g)$, calculated using the parameterised and observed PSDs at the two frequencies. The PSDs used in the tables to calculate the integral ice optical properties are the same as those used in Fig. 8. For the comparisons shown in the tables, the tropical parameterised PSDs are used for the calculations shown in the tables, as this parameterisation generates higher number concentrations of larger ice crystals than does the mid-latitude parameterisation [62]. Interestingly, Table 1 shows that at 874 GHz, the bulk extinction coefficients calculated using the parameterisation and observed PSD 2 differ by only about 12%. This is because the parameterisation for the same amount of ice mass generates enough smaller ice crystals to predict similar bulk extinction coefficients to those of the observed PSDs, owing to the maximum contributions to the PSDs at this frequency occurring at smaller ice crystal sizes than several centimetres. However, the integral optical properties ω_0 and g are significantly different between the parameterisation and the observed PSDs, as reflected in Table 1. The parameterisation would predict warmer cloud relative to the observed PSDs, as its bf value is smaller than the corresponding values obtained with the observed PSDs by about 10% (Table 3). At 89 GHz, there are major differences between the parameterised PSD bulk extinction coefficients and the corresponding coefficients calculated using the observed PSDs, and these differences are on the order of factors of three to four. Clearly, in this case, the cloud assuming the parameterised PSD, with all things being equal, would predict significantly warmer upwelling microwave radiation than if the observed PSDs were to be used, even though, as shown in Table 3, the bf values are similar at this frequency. At 89 GHz, the

large cm-sized ice aggregates become more important contributors to the bulk extinction coefficients than previously found at 874 GHz. The findings here suggest a further possible reason as to why simulated microwave emission appears to be warmer than observed microwave emission in some studies [63], which, in part, could be due to the assumed PSDs not being sufficiently broad.

To further improve the PSD parameterisation that might be used in NWP and climate models, it is of necessity to make greater use of the microphysical instrument deployed in Ref. [58] in future field campaigns. Very broad PSDs do occur in natural ice clouds, albeit under perhaps unusual conditions as reported in Ref. [58]. However, to predict such cm-sized ice aggregates in NWP and climate models, it is important to construct improved PSD parameterisations and single-scattering databases should consider cm-sized (i.e. up to ~ 5 cm) ice aggregates to take into account the occurrence of possible very broad PSDs.

Table 1.

Comparisons between the bulk integral ice optical properties (β_{ext}, ω_0, g) obtained from the moment estimation parameterisation of Ref. [26] using the tropical PSDs (F07) and the observed PSDs at 874 GHz. The same IWC and T_c values were used as in Fig. 8 to generate the tropical PSD.

PSD	β_{ext} m^{-1}	ω_0	g
F07	0.01644	0.8521	0.7046
Observed PSD1	0.01664	0.6689	0.8248
Observed PSD2	0.01849	0.6869	0.8101

Table 2.

The same as Table 1 but at 89 GHz.

PSD	β_{ext} m^{-1}	ω_0	g
F07	0.004036	0.9894	0.5408
Observed PSD1	0.01461	0.9733	0.5796
Observed PSD2	0.01537	0.9757	0.5630

Table 3.

Comparisons of the approximate backscattered fraction, bf, where bf ~ (1 - ω_0g), between the moment estimated tropical PSD (F07) and the observed PSDs at 89 and 874 GHz.

PSD	bf (874 GHz)	bf (89 GHz)
F07	0.3996	0.4649
Observed PSD1	0.4483	0.4358
Observed PSD2	0.4435	0.4507

7. Conclusions and discussion

In this paper, a three-component model for ice cloud in the microwave has been proposed. The components of this model consist of the hexagonal ice column of aspect ratio unity, the ten-column aggregate model, and the Voronoi particle. The Voronoi model was constructed so as to follow observed density–dimension relationships that are generally found in cirrus. The light scattering methodologies discussed in Part I have been applied to compute the single-scattering properties of the first two members of this model between the frequencies of 89 and 874 GHz. The single-scattering properties predicted by these three models were compared with already existing single-scattering databases in the microwave region, which are based on other ice crystal models. The single-scattering properties predicted by the three-component model

members were compared to those computed while assuming the ten- and five-plate aggregate model, the eight-column aggregate, and the six-branched hollow bullet rosette.

The geometry of the second member of the three-component model was approximated at size parameters less than about 18 by the equal area ratio hexagonal ice column. This allowed for very rapid computation of the single-scattering properties using the T-matrix method applied to a non-axisymmetric ice particle in random orientation. At size parameters greater than 18, the actual geometry of the model was used to generate the single-scattering properties by applying the Monte Carlo ray-tracing method. Firstly, the bulk integral ice optical properties (i.e. β_{ext}, and the co-albedo, $1 - \omega_0$) were compared to understand if members of the three-component model bounded the same properties predicted by the other ice crystal models. It was found that, in general, in the case of β_{ext}, the three-component model did bound some or all of the other bulk integral ice optical properties at frequencies between 89 and 874 GHz. At the sub-mm-wave frequencies, the three-component model did bound most of the other ice crystal models, apart from the six-branched hollow bullet rosette. As frequency decreased and, therefore, ice crystal absorption, owing to decreasing values in the imaginary ice refractive index, the proposed model members, at the lowest frequency of 89 GHz, did not generally bound the six-branched hollow bullet rosette.

In the case of the co-albedo, at 874 GHz, the proposed model members did generally bound the other ice crystal models when the mean mass-weighted size, D_{mmw}, > 400 μm. At this frequency, the second member of the three-component model was found to scatter similarly to the five-plate aggregate. It was also found that the shape of the PSD was as important as the assumed ice crystal shape, as significantly different values of β_{ext} and $1-\omega_0$ could be found for PSDs that gave similar D_{mmw} values but were different in shape. It is therefore of importance to assume representative PSDs in the remote sensing of ice cloud microphysical and

macrophysical properties in the microwave region and not just the assumed ice crystal shape.

The members of the three-component model were also found to generally bound the other ice crystal models when the size-averaged scattering matrix elements were compared at the two frequencies of 89 and 874 GHz. At 89 GHz, this bounding of the proposed model members to most of the other ice crystal models was found to generally be the case when the P_{11}, P_{12}, P_{22}, and P_{33} elements were compared. For the P_{12} element, the three-component model was mostly divergent from the six-branched hollow bullet rosette at scattering angles of around 80°. At 874 GHz, there were similar findings at this frequency to those found at 89 GHz. One of the differences that was found for the P_{12} element was that the eight-column aggregate was most divergent from the other chain-like aggregate models at scattering angles between about 25° and less than about 100°. Thus, discriminating ice crystal complexity using linear polarisation at sub-mm-wave frequencies might be possible in distinguishing compact ice aggregates from chain-like ice crystals. If these particles were horizontally oriented, then it would be expected that such differences would become even greater. However, further polarised radiative transfer studies are required to confirm this finding. Generally, it is found that approximating the ten-branched hexagonal ice aggregate model through the equal area ratio hexagonal column did not cause any major detriment to the single-scattering property comparisons; thus, this approximation will allow for extremely rapid computation of randomly oriented ice crystals using the T-matrix method to take into account its analytic orientation averaging procedures. A further observation from these analyses was that the Voronoi and six-branched bullet rosette models appear to have similar single-scattering properties. This means that it might be possible to simulate ice models with observed effective density–size relationships with simpler hollow bullet rosettes.

The above findings indicate that the proposed model generally bound most of the other ice crystal models assumed in this paper. This means that the three-component model can be

weighted at each size bin in the PSD, to obtain equivalent microwave radiances in a similar way to Ref. [28]. This assertion will be tested in Part III, where microwave observations between 89 and 874 GHz, obtained from a number of ice cloud cases, will be used to test the three-component model presented in this paper. Equally notable was the finding that about 5 cm-sized ice crystal aggregates may need to be considered in future ice crystal single-scattering databases, as current parameterisations of the PSD do not take into account the possibility of very broad PSDs. Such PSDs have been observed to occur in natural ice aggregating cloud. Therefore, further field campaigns are necessary to observe the frequency of occurrence of this process using microphysical instrumentation that is capable of measuring cm-sized (i.e. ~ 5 cm) aggregating ice crystals to further aid PSD parameterisations and ice crystal single-scattering databases.

APPENDIX

Details of the Voronoi model electromagnetic calculations are given here. The method of applying Voronoi tessellations to construct 3D particle shapes has already been described in Ref. [36], and as discussed in that reference, the Voronoi model can be constructed so as to follow any density–dimension relationship. As discussed in Section 1, the Voronoi model used here follows the effective density–size relationship, ρ_e, found by Ref. [37] using in-situ data obtained in the mid-latitudes in cold cirrus, and they found this to be $\rho_e=0.049D^{-1.0}$, for $D > 70$ μm. A figure showing the Voronoi construction at the example frequency of 664 GHz is shown in Figs. A.1 and A.2.

Figure A.1. The Voronoi particle model, where model numbers between 1 and 25 represent orientation-averaged maximum dimensions between 0.4 and 2559 μm, respectively. Model numbers 1 to 12 are the same model as shown above but for orientation-averaged maximum dimensions between 0.4 and 70 μm.

Figure A.2. The same as Fig. A.1 but for particle model numbers between 25 and 31, which represent orientation-averaged maximum dimensions between 2559 and 15,000 μm.

Shown in Fig. A.1 is the model geometry for very small dimensions; such dimensions will be of no radiative importance in the microwave or sub-millimetre spectral regions. However, such dimensions will be of importance in the solar region of the spectrum and, therefore, it is important to show the full model that can be applied across the electromagnetic spectrum while consistently using the same microphysics. The microphysics of each of the model configurations presented in Figs. A.1 and A.2 is given in Table A.1. It can be seen from Table A.1 that the Voronoi model conforms to observations of ρ_e and area ratio (previously defined in Section 1) very well [37, 13, 44] and, thus, should be a useful model to apply across the electromagnetic spectrum of relevance to Earth observation. Indeed, in Table A.2, the model is shown to follow the chosen effective density–size relationship very well.

Table A.1. The microphysics of the Voronoi model, where Element is the number of polyhedral particles that comprise each shape, D is the maximum dimension (averaged over 100 random orientations), the Area rat (area ratio) is averaged over 100 random orientations and, lastly, the ratio of the ρ_e in each DDSCAT and FDTD cell to the model ρ_e is also provided.

No.	Shape	Element	D μm	ρ_e Kg m^{-3}	Area rat	ρ_{e_cell}/ρ_e
1–12	1	3	0.4–70	629.2	0.853	1.0
13	2	9	147.3	333.1	0.639	1.0
14	3	23	224.9	239.2	0.565	1.0
15	4	45	313.6	172.6	0.493	1.0
16	5	77	419.2	123.6	0.458	1.0
17	6	113	499.9	107.0	0.437	1.0
18	7	169	622.6	82.8	0.401	1.0
19	8	221	751.6	61.6	0.363	1.0
20	9	298	866.7	54.1	0.347	1.0
21	10	340	964.4	44.8	0.330	1.0
22	11	488	1080	45.2	0.324	1.0
23	12	822	1400	34.2	0.322	1.0
24	13	1254	1754	26.6	0.313	1.0
25	14	2767	2559	18.9	0.282	1.0
26	14'	2767	3500	13.8	0.281	0.731
27	14'	2767	5000	9.68	0.281	0.512
28	14'	2767	7500	6.45	0.281	0.341
29	14'	2767	10,000	4.84	0.281	0.256
30	14'	2767	12,000	4.03	0.281	0.213
31	14'	2767	15,000	3.23	0.281	0.171

Table A.2. A comparison between the Voronoi model and Ref. [37] ρ_{ev} and ρ_e values, respectively.

D µm	ρ_{ev} kg m^{-3}	ρ_e kg m^{-3}
70	629.2	700.0
147.3	333.1	332.7
224.9	239.2	217.9
313.6	172.6	156.3
419.2	123.6	116.9
499.9	107.0	98.0
622.6	82.8	78.7
751.6	61.6	65.2
866.7	54.1	56.5
964.4	44.8	50.8
1080	45.2	45.4
1400	34.2	35.0
1754	26.6	27.9
2559	18.9	19.1
3500	13.8	14.0
5000	9.68	9.80
7500	6.45	6.53
10,000	4.84	4.90
12,000	4.03	4.08
15,000	3.23	3.27

The numerical settings for the DDSCAT calculations were as follows. The error tolerance was set at 1.0e-05, the maximum number of iterations was set at 300, the interaction cut-off parameter was set at 1.0e-02, the number of random orientations was 100, and dipole spacing (d) is selected to be $|m|kd \leq 1.0$, except for No.31 at 874 GHz (for No.31 at 874 GHz, $|m|kd = 1.23$). Grid spacing in the FDTD calculations is the same as that used in the DDSCAT calculations. Grid spacing was defined as follows:

No.24–27 for 874 GHz (grid spacing $\lambda/22.1 \leq d \leq \lambda/17.7$),

No.25–28 for 664 GHz (grid spacing $\lambda/21.4 \leq d \leq \lambda/15.5$),

No.26–30 for 448 GHz (grid spacing $\lambda/23.2 \leq d \leq \lambda/14.4$),

No.27–31 for 325 GHz (grid spacing $\lambda/22.4 \leq d \leq \lambda/15.8$),

No.28–31 for 243 GHz (grid spacing $d = \lambda/20.0$),

No.28–31 for 229 GHz (grid spacing $\lambda/21.8 \leq d \leq \lambda/20.0$),

No.29–31 for 183.31 GHz (grid spacing $d = \lambda/20.0$),

No.29–31 for 165.5 GHz (grid spacing $\lambda/22.0 \leq d \leq \lambda/20.0$),

where λ is the incident wavelength.

References

[1] Klein, U., Loiselet, M., Mason, G., Gonzalez, R., Brandt, M., ESA's Ice Cloud Imager on Metop Second Generation, In proceedings EGU General Assembly Conference Abstracts, 18, Apr 2016, page 17750, 2016.
[2] Fox, S., Lee, C., Moyna, B., Philipp, M., Rule, I., Rogers, S., King, R., Oldfield, M., Rea, S., Henry, M., Wang, H., and Harlow, R. C.: ISMAR: an airborne submillimetre radiometer, *Atmos. Meas. Tech.*, doi:10.5194/ amt-10-477-2017, 2017.
[3] Evans, K. F., Walter, S. J., Heymsfield, A. J., and Deeter, M. N., Modeling of submillimeter passive remote sensing of cirrus clouds, *J. Appl. Meteorol.*, **37**(1998), 184– 205.
[4] Wang, J., Liu, G., Spinhirne, J., Racette, P., and Hart, W., Observations and retrievals of cirrus cloud parameters using multichannel millimeter-wave radiometric measurements, *J. Geophys. Res.*, **106**(2001), 15,251– 15,263.
[5] Vanek, M. D., et al., Far infrared sensor for cirrus (FIRSC) , An aircraft based FTS to measure the earth radiance spectrum, *Appl. Opt.*, **40**(2001), 2169–2176.
[6] Evans, K. F., Walter, S. J., and Heymsfield, A. J., Submillimeter-Wave Cloud Ice Radiometer: Simulations of retrieval algorithm performance, *J. Geophys. Res.*, **107**(2002), 10.1029/2001JD0007.
[7] Baran, Anthony. J., Bodas-Salcedo, A., Cotton, R. and Lee, C., Simulating the equivalent radar reflectivity of cirrus at 94 GHz using an ensemble model of cirrus ice crystals: a test of the Met Office global numerical weather prediction model. *Q.J.R. Meteorol. Soc.*, **137**(2011), 1547–1560, doi: 10.1002/qj.870.

[8] Waliser, D. E., Li, J.-L. F., Woods, C. P., Austin, R. T., Bacmeister, J., Chern, J., Del Genio, A., Jiang, J. H., Kuang, Z., Meng, H., Minnis, P., Platnick, S., Rossow, W. B., Stephens, G. L., Sun-Mack, S., Tao, W.-K., Tompkins, A. M., Vane, D. G., Walker, C., and Wu, D.: Cloud ice: A climate model challenge with signs and expectations of progress, J. Geophys. Res., **114**(2009), D00A21,doi:10.1029/2008JD010015.

[9] Stein, T. H. M., Parker, D. J., Hogan, R. J., Birch, C. E., Holloway, C. E., Lister, G. M. S., Marsham, J. H. and Woolnough, S. J., The representation of the West African monsoon vertical cloud structure in the Met Office Unified Model: an evaluation with CloudSat. Q.J.R. Meteorol. Soc., **141**(2015), 3312–3324. doi:10.1002/qj.2614

[10] IPCC, 2013: Climate Change 2013: The Physical Science Basis. Contribution of Working Group I to the Fifth Assessment Report of the Intergovernmental Panel on Climate Change [Stocker, T.F., D. Qin, G.-K. Plattner, M. Tignor, S.K. Allen, J. Boschung, A. Nauels, Y. Xia, V. Bex and P.M. Midgley (eds.)]. Cambridge University Press, Cambridge, United Kingdom and New York, NY, USA, 1535 pp, doi:10.1017/CBO9781107415324.

[11] Westbrook, C. D., R. C. Ball, P. R. Field, and A. J. Heymsfield, A theory of growth by differential sedimentation with application to snowflake formation. Physical Review E, **70**(2004), 021403.1-021403.7, doi:10.1103/PhysRevE.70.021403.

[12] Schmitt, C. and A. Heymsfield, The Dimensional Characteristics of Ice Crystal Aggregates from Fractal Geometry. *J. Atmos. Sci.*, **67**(2010), 1605–1616, doi: 10.1175/2009JAS3187.1.

[13] Field, P., J. Heymsfield, A. Bansemer, and C. Twohy, Determination of the Combined Ventilation Factor and Capacitance for Ice Crystal Aggregates from Airborne Observations in a Tropical Anvil Cloud. *J. Atmos. Sci.*, **65**(2008), 376–391, doi: 10.1175/2007JAS2391.1.

[14] Liu, G., A Database of Microwave Single-Scattering Properties for Nonspherical Ice Particles. *Bull. Amer. Meteor. Soc.*, **89**(2008), 1563–1570. doi: http://dx.doi.org/10.1175/2008BAMS2486.1

[15] Hong, G., Yang, P., Baum, B. A., Heymsfield, A. J., Weng, F., Liu, Q., Heygster, G., and Buehler, S. A., Scattering database in the millimeter and submillimeter wave range of 100 - 1000 GHz for nonspherical ice crystals. *Journal of Geophysical Research-Atmospheres*, **114**(2009), D06201, DOI: 10.1029/2008JD010451.

[16] Hogan, R. J., and Westbrook, C. D., Equation for the microwave backscatter cross section of aggregate snowflakes using the self-similar Rayleigh–Gans approximation. *J. Atmos. Sci.*,**71**(2014), 3292–3301, doi:10.1175/JAS-D-13-0347.1

[17] Baran, A. J., Cotton, R., Furtado, K., Havemann, S., Labonnote, L.-C., Marenco, F., Smith, A. and Thelen, J.-C., A self-consistent scattering model for cirrus. II: The high and low frequencies. *Q.J.R. Meteorol. Soc.*, **140**(2014), 1039–1057. doi:10.1002/qj.2193.

[18] Geer, A. J. and Baordo, F., Improved scattering radiative transfer for frozen hydrometeors at microwave frequencies, *Atmos. Meas. Tech.*, **7**(2014), 1839–1860, doi:10.5194/amt-7-1839-2014.

[19] Eriksson, P., Jamali, M., Mendrok, J., and Buehler, S. A.: On the microwave optical properties of randomly oriented ice hydrometeors, *Atmos. Meas. Tech.*, **8**(2015), 1913-1933, doi:10.5194/amt-8-1913-2015.

[20] Botta, G., K. Aydin, J. Verlinde, A. E. Avramov, A. S. Ackerman, A. M. Fridlind, G. M. McFarquhar, and M. Wolde, Millimeter wave scattering from ice crystals and their aggregates: Comparing cloud model simulations with X- and Ka-band radar measurements, *J. Geophys. Res.*, **116**(2011), D00T04, doi:10.1029/2011JD015909.

[21] Ding, J., Bi, L., Yang, P., Kattawar, G. W., Weng, F., Liu, Q., Greenwald, T., Single-scattering properties of ice particles in the microwave regime: Temperature effect on the ice refractive index with implications in remote sensing, Journal of Quantitative Spectroscopy and Radiative Transfer, **190**(2017), 26-37, ISSN 0022-4073, http://dx.doi.org/10.1016/j.jqsrt.2016.11.026.

[22] Lu, Y., Jiang, Z., Aydin, K., Verlinde, J., Clothiaux, E. E., and Botta, G.: A polarimetric scattering database for non-spherical ice particles at microwave wavelengths, *Atmos. Meas. Tech.*, **9**(2016), 5119-5134, doi:10.5194/amt-9-5119-2016.

[23] Yang, P. and Liou, K. N, Single-scattering properties of complex ice crystals in terrestrial atmosphere, *Contr. Atmos. Phys.*, **71**(1998), 223–248.

[24] Baum, B., Heymsfield, A., Yang, P., and Bedka, S., Bulk Scattering Properties for the Remote Sensing of Ice Clouds. Part I: Microphysical Data and Models. *J. Appl. Meteor.*, **44**(2005), 1885–1895, doi: 10.1175/JAM2308.1.

[25] Baran, A. J. and Labonnote, L.–C., A self-consistent scattering model for cirrus. 1: The solar region, *Q. J. Roy. Meteor. Soc.*,**133**(2007), 1899–1912.

[26] Field, P., Heymsfield, A. J., and Bansemer, A., Snow Size Distribution Parameterization for Midlatitude and Tropical Ice Clouds. *J. Atmos. Sci.*, **64**(2007), 4346–4365, doi: 10.1175/2007JAS2344.1.

[27] Vidot, J., Baran, A. J., and Brunel P., A new ice cloud parameterization for infrared radiative transfer simulation of cloudy radiances: Evaluation and optimization with IIR observations and ice cloud profile retrieval products. *J. Geophys. Res. Atmos.*, **120**(2015), 6937–6951. doi: 10.1002/2015JD023462.

[28] Letu, H., Ishimoto, H., Riedi, J., Nakajima, T. Y., C.-Labonnote, L., Baran, A. J., Nagao, T. M., and Sekiguchi, M., Investigation of ice particle habits to be used for ice cloud remote sensing for the GCOM-C satellite mission, *Atmos. Chem. Phy*s., **16**(2016), 12287-12303, doi:10.5194/acp-16-12287-2016.

[29] Baran, A. J., Evelyn Hesse, Odran Sourdeval, The applicability of physical optics in the millimetre and sub-millimetre spectral region. Part I: The ray tracing with diffraction on facets method. *J. Quant. Spectrosc. Radiat. Transf.* **190**(2017), 13–25, doi:10.1016/j.jqsrt.2016.12.030.

[30] Hesse, E., Modelling diffraction during ray tracing using the concept of energy flow lines. *J. Quant. Spectrosc. Radiat. Transf.* **109**(2008), 1374–1383.

[31] Borovoi, A. G., and Grishin, I. A., Scattering matrices for large ice crystal particles, *J. Opt. Soc. Am. A* **20**(2003), 2071-2080.

[32] Bi, L., Yang, P., Kattawar, G. W., Hu, Y.-X. and Baum, B. A., Scattering and absorption of light by ice particles: Solution by a new physical-geometric optics hybrid method. *J. Quant. Spectrosc. Radiat. Transfer*, **112**(2011), 1492-1508, doi:10.1016/j.jqsrt.2011.02.015.

[33] Muinonen, K., Lumme, K., Peltoniemi, J., and Irvine, W. M., Light scattering by randomly oriented crystals, *Appl. Opt*. **28**(1989), 3051-3060.

[34] Bi, L., and Yang, P., Accurate simulation of the optical properties of atmospheric ice crystals with the invariant imbedding T-matrix method. *J. Quant. Spectrosc. Radiat. Transfer*, **138**(2014), 17–35, doi:10.1016/j.jqsrt.2014.01.013.

[35] Yang, P., and Liou, K. N., Geometric-optics-integral-equation method for light scattering by nonspherical ice crystals. *Appl. Opt.*, **35**(1996), 6568–6584, doi:10.1364/AO.35.006568.

[36] Ishimoto, H., Masuda, K., Mano, Y., Orikasa, N., and Uchiyama, A., Irregularly shaped ice aggregates in optical modeling of convectively generated ice clouds, *J. Quant. Spectrosc. Radiat. Transfer* , **113**(2012), 632–643.

[37] Cotton, R. J., Field, P. R., Ulanowski, Z., Kaye, P. H., Hirst, E., Greenaway, R. S., Crawford, I., Crosier, J. and Dorsey, J., The effective density of small ice particles obtained from in situ aircraft observations of mid-latitude cirrus. *Q.J.R. Meteorol. Soc*., **139**(2013),1923–1934. doi:10.1002/qj.2058.

[38] Draine, B. T., and Flatau, P. J., Discrete-dipole approximation for scattering calculations, *J. Opt. Soc. Am. A Opt. Image Sci*., **11**(1994), 1491–1499.

[39] Macke, A., Mueller, J., and Raschke, E., Single Scattering Properties of Atmospheric Ice Crystals, *Journal of the Atmospheric Sciences*, **53**(1996), 19, 2813-2825.

[40] Havemann S., and Baran, A. J., Extension of T-matrix to scattering of electromagnetic plane waves by non-axisymmetric dielectric particles: application to hexagonal ice cylinders, *J. Quant. Spectrosc. Radiat. Transfer*, **70**(2001), 139-158.

[41] Mishchenko, M. I.,Travis, L. D., Capabilities and limitations of a current FORTRAN implementation of the T-matrix method for randomly oriented, rotationally symmetric scatterers, *J. Quant. Spectrosc. Radiat. Transfer*, **60**(1998), 309-324.

[42] Schnaiter, M., Järvinen, E., Vochezer, P., Abdelmonem, A., Wagner, R., Jourdan, O., Mioche, G., Shcherbakov, V. N., Schmitt, C. G., Tricoli, U., Ulanowski, Z., and Heymsfield, A. J., Cloud chamber experiments on the origin of ice crystal complexity in cirrus clouds, Atmos. Chem. Phys., **16**(2016), 5091-5110, doi:10.5194/acp-16-5091-2016.

[43] Baran, A. J., A review of the light scattering properties of cirrus. *J. Quant. Spectrosc. Radiat. Transfer*, **110**(2009), 1239–1260.

[44] Fu, Q., A new parameterization of an asymmetry factor of cirrus clouds for climate models, *J. Atmos. Sci*., **64**(2007), 4140, doi:10.1175/2007JAS2289.1.

[45] Um, J. and McFarquhar, G. M., Single-scattering properties of aggregates of bullet rosettes in cirrus, *J. Appl. Meteorol. Clim.*, **46**(2007), 757–775, doi:10.1175/JAM2501.1.

[46] Um, J. and McFarquhar, G. M., Single-scattering properties of aggregates of plates, *Q. J. Roy. Meteorol. Soc*, **135**(2009), 291–304, doi:10.1002/qj.378.

[47] Baran, A. J., Furtado, K., Labonnote, L.-C., Havemann, S., Thelen, J.-C., and Marenco, F., On the relationship between the scattering phase function of cirrus and the atmospheric state, *Atmos. Chem. Phys*., **15**(2015), 1105-1127, doi:10.5194/acp-15-1105-2015.

[48] Kuhn, T., Heymsfield, A. J., In Situ Balloon-Borne Ice Particle Imaging in High-Latitude Cirrus, *Pure and Applied Geophysics*, **173**(2016), 3065-3084.

[49] Mätzler, C., Microwave dielectric properties of ice. Thermal microwave radiation -Applications for remote sensing, *Electro-magn., Waves Ser*., vol. 52, edited by: C. Mätzler, Inst. Eng.Technol., Stevenage, UK, Sect. 5.3, 455–462(2006).

[50] Foot, J. S., Some observations of the optical properties of clouds. II: Cirrus. *Q.J.R. Meteorol. Soc*., **114**(1988) 145–164. doi:10.1002/qj.49711447908.

[51] Baran, A., Hill, P., Furtado, K., Field, P., and Manners, J., A Coupled Cloud Physics–Radiation Parameterization of the Bulk Optical Properties of Cirrus and Its Impact on the Met Office Unified Model Global Atmosphere 5.0 Configuration. *J. Climate*, **27**(2014), 7725–7752, doi: 10.1175/JCLI-D-13-00700.1.

[52] Mishchenko, M. I., and Travis, L. D., Light scattering by polydispersions of randomly oriented spheroids with sizes comparable to wavelengths of observation, *Appl. Opt.*, **33**(1994), 7206-7225.

[53] Iwabuchi H., and Yang P.,Temperature dependence of ice optical constants: Implications for simulating the single-scattering properties of cold ice clouds, *J. Quant. Spectrosc. Radiat. Transfer,* **112**(2011), 2520-2525 .

[54] Tang, G., Yang, P., Wu, D. L., Sensitivity study of ice crystal optical properties in the 874 GHz submillimeter band, Journal of Quantitative Spectroscopy and Radiative Transfer, http://dx.doi.org/10.1016/j.jqsrt.2015.12.008 (2016).

[55] Yang P., Bi L., Baum B. A., Liou K.-N., Kattawar G. W., Mishchenko M. I., and Cole B, Spectrally consistent scattering, absorption, and polarization properties of atmospheric ice crystals at wavelengths from 0.2 μm to 100 μm, *J. Atmos. Sci.*, **70**(2013), 330-347.

[56] Miao, J., Johnsen, K.-P., Buehler, S., and Kokhanovsky, A., The potential of polarization measurements from space at mm and sub-mm wavelengths for determining cirrus cloud parameters, *Atmos. Chem. Phys.*, **3**(2003), 39-48, https://doi.org/10.5194/acp-3-39-2003.

[57] Doherty, A. M., Sreerekha, T. R., O'Keeffe, U. M. and English, S. J., Ice hydrometeor microphysical assumptions in radiative transfer models at AMSU-B frequencies. *Q.J.R. Meteorol. Soc.*, **133**(2007), 1205–1212, doi:10.1002/qj.84.

[58] Lawson, R., Stewart, R., and Angus, L., Observations and Numerical Simulations of the Origin and Development of Very Large Snowflakes. *J. Atmos. Sci.*, **55**(1998), 3209–3229, doi: 10.1175/1520-0469(1998)055<3209:OANSOT>2.0.CO;2.

[59] Baran, A. J., Connolly, P. J., Heymsfield, A. J. and Bansemer, A. , Using in situ estimates of ice water content, volume extinction coefficient, and the total solar optical depth obtained during the tropical ACTIVE campaign to test an ensemble model of cirrus ice crystals. *Q.J.R. Meteorol. Soc.*, 137(2011), 199–218. doi:10.1002/qj.731

[60] Furtado, K., Field, P. R., Cotton, R. and Baran, A. J., The sensitivity of simulated high clouds to ice crystal fall speed, shape and size distribution. *Q.J.R. Meteorol. Soc.*, **141**(2015), 1546–1559. doi:10.1002/qj.2457

[61] Houze R. A., Hobbs P.V., Herzegh P.H., Parsons D.B., Size distributions of precipitation particles in frontal clouds, *J. Atmos. Sci.*, **36**(1979), 156–162.

[62] Di Michele, S., Ahlgrimm, M., Forbes, R., Kulie, M., Bennartz, R., Janisková, M. and Bauer, P., Interpreting an evaluation of the ECMWF global model with CloudSat observations: ambiguities due to radar reflectivity forward operator uncertainties. *Q.J.R. Meteorol. Soc.*, **138**(2012), 2047–2065. doi:10.1002/qj.1936

[63] Johnston, M. S., Holl, G., Hocking, J., Cooper, S. J., and Chen, D, Simulating the effects of mid- to upper-tropospheric clouds on microwave emissions in EC-Earth using COSP, *Atmos. Meas. Tech. Discuss.*, 8(2015), 11753-11777, doi:10.5194/amtd-8-11753-2015.